Potential of an Alumina-Supported Ni_3Fe Catalyst in the Methanation of CO_2: Impact of Alloy Formation on Activity and Stability

Benjamin Mutz,[†,‡] Michael Belimov,[§] Wu Wang,[∥] Paul Sprenger,[†] Marc-André Serrer,[†,‡] Di Wang,[∥,⊥] Peter Pfeifer,[§] Wolfgang Kleist,[*,†,‡,#] and Jan-Dierk Grunwaldt[*,†,‡]

[†]Institute for Chemical Technology and Polymer Chemistry, Karlsruhe Institute of Technology (KIT), D 76131 Karlsruhe, Germany
[‡]Institute of Catalysis Research and Technology, [§]Institute for Micro Process Engineering, [∥]Institute of Nanotechnology, [⊥]Karlsruhe Nano Micro Facility, Karlsruhe Institute of Technology (KIT), D 76344 Eggenstein Leopoldshafen, Germany

ABSTRACT: A promising bimetallic 17 wt % Ni_3Fe catalyst supported on γ Al_2O_3 was prepared via homogeneous deposition–precipitation for the application in the methanation of CO_2 to gather more detailed insight into the structure and performance of the catalyst compared to state of the art methanation systems. X ray diffraction (XRD) analysis, detailed investigations using scanning transmission electron microscopy (STEM) combined with energy dispersive X ray spectroscopy analysis (EDX) of single particles as well as larger areas, high resolution transmission electron microscopy (HRTEM) imaging, temperature programmed reduction (H_2 TPR), and in depth interpretation of Raman bands led to the conclusion that a high fraction of the Ni and Fe formed the desired Ni_3Fe alloy resulting in small and well defined nanoparticles with 4 nm in size and a dispersion of 24%. For comparison, a monometallic catalyst with similar dispersion using the same preparation method and analysis was prepared. Using a fixed bed reactor, the Ni_3Fe catalyst showed better low temperature performance compared to a monometallic Ni reference catalyst, especially at elevated pressures. Long term experiments in a microchannel packed bed reactor under industrially relevant reaction conditions in competition with a commercial Ni based methanation catalyst revealed an improved performance of the Ni_3Fe system at 358 °C and 6 bar involving enhanced conversion of CO_2 to 71%, selectivity to CH_4 > 98%, and most notably a high stability. Deactivation occurred only at lower temperatures, which was related to carbon deposition due to an increased CO production. Kinetic measurements were compared with literature models derived for Ni/Al_2O_3 catalysts, which fit well but underestimate the performance of the Ni_3Fe system, emphasizing the synergetic effect of Ni and Fe.

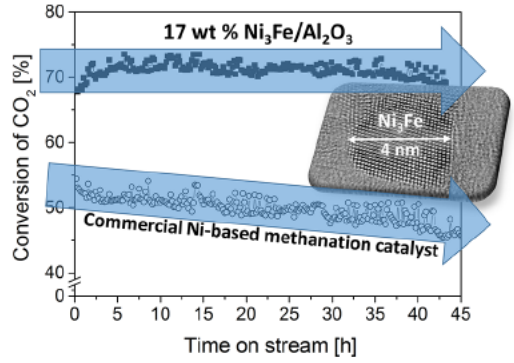

KEYWORDS: *Ni_3Fe alloy, CO_2 methanation, high stability, long term performance, kinetics*

1. INTRODUCTION

The methanation of CO_2 plays an important role in future power systems based on renewable energy. Due to the fluctuating supply of wind and solar energy, storage systems are needed to stabilize the electricity grid.[1−6] Synthetic natural gas (SNG) produced within the power to gas process is a promising and suitable chemical energy carrier due to its long term storage ability and the existing infrastructure in form of the natural gas grid.[7−11] The synthesis of CH_4 from CO_2 and renewable H_2 via the Sabatier reaction (eq 1) is a well known process utilizing Ni based catalysts.[12−15]

$$CO_2 + 4H_2 \rightleftharpoons CH_4 + 2H_2O \quad \Delta H_{298K} = -165\ \text{kJ mol}^{-1} \tag{1}$$

$$CO_2 + H_2 \rightleftharpoons CO + H_2O \quad \Delta H_{298K} = -41\ \text{kJ mol}^{-1} \tag{2}$$

The reaction is exothermic and thermodynamically favored between 200−500 °C.[16] At about 450 °C, the endothermic back reaction and the reverse water−gas shift reaction (eq 2) diminish the CO_2 conversion and produce CO as a byproduct, respectively. For more details about the thermodynamics of the reaction, the reader is referred to the work of Gao et al.[16] Details about the mechanism of the methanation reaction are given in review articles (e.g., refs 12−14). Due to the exothermic reaction, the produced heat may cause the formation of hot spots. Usually, the catalyst bed is diluted with inert material such as SiC. Structured fixed bed reactors with zones of optimized dilution are also possible.[17] For a better temperature control, microstructured reactors with altering cooling channels have been developed.[18−20]

Doping of these Ni catalysts with a second metal can improve both the catalytic performance and the stability of the catalyst.[13,14] Enhanced low temperature performance and stability was reported using complex supported Ni MgO systems[21−25] Doping a Ni catalyst with noble metals leading to Ni−Ru[26,27] or Ni−Pd[28] systems was reported to enhance the activity and stability. These are interesting and promising catalyst systems on an academic level, but industrially, Ni/Al_2O_3 doped with CaO or MgO is still the most commonly used system due to its low cost. Recently, NiFe alloy catalysts have been reported to claim a significantly better catalytic performance due to an improved CO dissociation as predicted by DFT calculations.[29,30] Experimental results showed that the addition of Fe improved the methanation of CO compared to the monometallic Ni catalysts, and an excellent catalytic performance was reported.[31,32] Furthermore, bimetallic NiFe catalysts achieved higher performance in the methanation of CO_2[33−36] as well as combinations of CO and CO_2[33,37] compared to monometallic Ni catalysts. A monometallic Fe catalyst was significantly less active than the Ni catalyst.[33,35] The influence of dopants such as Fe, Co, Cu, Zr, Y, and Mg on Ni catalysts in the methanation of CO_2 was experimentally investigated by Hwang et al.[34] and Ren et al.[36] The superior performance of the NiFe catalyst among the other dopants was ascribed to the weak metal−support interaction and an optimal CO dissociation energy at the surface of the alloy.[34,36] NiFe catalysts show the lowest peak temperature in temperature programmed surface reactions compared to monometallic catalysts or other bimetallic systems, which experimentally supports the optimal CO dissociation energy in the CO_2 methanation.[34] The optimum Ni/Fe ratio in the desired alloy was found to be around 3, as reported by various studies.[31,33,35,37]

However, long term stability and performance tests under harsh and industrially relevant reaction conditions combined with in depth structural investigations are necessary to evaluate the potential of the Ni_3Fe system in methanation applications. Such structure−performance relationships require uniformly sized and well dispersed Ni_3Fe alloy nanoparticles on the support material also allowing to monitor changes and modifications of the active material after the reaction.

In the present study, advances with respect to the preparation of the catalyst, new insights into its structural properties, and the catalytic potential at elevated pressures are reported. The Ni_3Fe catalyst was prepared via a homogeneous deposition−precipitation method on an Al_2O_3 support that is suitable to obtain small and well dispersed metal nano particles.[38−41] This catalyst and, for comparison, a mono metallic Ni reference catalyst were well characterized using X ray diffraction (XRD), scanning transmission electron micros copy (STEM) combined with energy dispersive X ray spec troscopy analysis (EDX), high resolution transmission electron microscopy (HRTEM), temperature programmed reduction with H_2 (H_2 TPR), and Raman spectroscopy. A combination of these methods was important to prove the formation of the desired Ni_3Fe alloy. The catalytic performance in the methanation of CO_2 was screened in a custom made continuous flow laboratory setup equipped with a tubular packed bed reactor with diluted catalyst in the temperature range of 200−450 °C at 1 and 10 bar. Additionally, long term stability tests under industrially relevant conditions were performed in a microchannel packed bed reactor setup for the Ni_3Fe catalyst in comparison to a commercial Ni based methanation catalyst to compare the results and to draw conclusions concerning the potential and the limitations of the bimetallic Ni_3Fe system.

2. EXPERIMENTAL SECTION

2.1. Catalyst Preparation. The bimetallic Ni_3Fe/Al_2O_3 catalyst and a monometallic Ni/Al_2O_3 reference system were both prepared via homogeneous deposition−precipita tion[40,42,43] with an intended total metal loading of 20 wt %. The synthesis mixture consisted of a 0.3 mol L^{-1} aqueous solution of the nitrate precursors ($(Ni(NO_3)_2{\cdot}6\ H_2O$ and $Fe(NO_3)_3{\cdot}9\ H_2O$ both Merck, ≥ 99%) with $n(Ni)/n(Fe) = 3$ and 7 equiv of urea (Carl Roth, crystalline, ≥99.6%). High surface area Al_2O_3 (1/8 in. pellets, Alfa Aesar, crushed to fine powder, calcined at 600 °C (5 K min^{-1}), 4 h) was suspended in the solution as catalyst support and stirred for 1 h at room temperature. The starting pH value was 6. Typically, 2 g of the catalyst was prepared in one batch consisting of 1.600 g of Al_2O_3, 1.502 g of nickel nitrate, 0.695 g of iron nitrate, 3.270 g of urea, and 230 mL of deionized water in the case of the bimetallic catalyst. The suspension was heated to 90 °C and stirred under reflux for 18 h (Ni/Al_2O_3) or 36 h (Ni_3Fe/Al_2O_3) at constant temperature. Afterward, the suspension was cooled to room temperature and stirred for another hour, reaching a pH value of 8. The solid was filtered off, washed with ca. 500 mL of deionized water, dried at 110 °C overnight, and calcined for 4 h at 500 °C (5 K min^{-1}) in static air. To characterize the catalyst in its reduced state, the samples were treated with 50% H_2/N_2 for 2 h at 500 °C (5 K min^{-1}) and stored under N_2 atmosphere.

2.2. Characterization. The elemental composition of the catalyst samples was determined by optical emission spectros copy using inductively coupled plasma (ICP OES). For this purpose, the samples were first digested in HCl + H_2SO_4 + H_2O_2 (2:2:1) at 240 °C for 12 h using a Berghof pressure digestion system DAB 2 and then the solution was analyzed using a PerkinElmer Optima 4300 DV System. The specific surface area of the catalyst powders was determined by N_2 physisorption according to the method of Brunauer, Emmet and Teller (BET) applying multi point measurements at a Rubotherm BELSORP mini II system. X ray diffraction (XRD) patterns were recorded using a PANalytical X'Pert PRO diffractometer with Ni filtered Cu Kα radiation (λ = 1.54060 Å) at 2Θ = 20−80° with a step size of 0.017° (0.51 s per scan step). The catalyst powders were measured ex situ in their reduced state on a rotating sample holder. The crystallite size was estimated using the Scherrer equation.

Electron microscopy investigations were also performed on the reduced catalyst samples. The powder samples were directly dispersed on copper grids covered with holey carbon film. The morphology and structure of the catalysts was characterized by HRTEM and high angle annular dark field (HAADF) STEM in a FEI Titan 80−300 microscope operating at 300 kV. The composition was estimated at specific locations using EDX with an EDAX S UTW EDX detector. Quantification of the EDX spectra and STEM EDX spectrum imaging were carried out by using TEM Image & Analysis (TIA 4.7 SP3 version) software. The size of the supported metal nanoparticles was estimated using ImageJ software fitting the particles with ellipsoid shapes. The metal dispersion was derived from their mean diameter by assuming spherical particle shape and by using element specific data such as the area occupied by surface metal atoms and the volume occupied by metal atoms in the bulk material.[44]

Temperature programmed reduction with H_2 (H_2 TPR) was performed using a Micromeritics AutoChem II 2920 chemisorption analyzer equipped with a thermal conductivity detector (TCD). Initially, 100 mg of the catalyst sample (mesh 100−200 μm) was placed in a U shaped quartz tube and pretreated at 500 °C (10 K min^{-1}) in 50 mL min^{-1} of 10% O_2/He followed by the TPR between 40−900 °C using 50 mL min^{-1} of 10% H_2/Ar.

Microscopic Raman spectroscopy was performed using a Renishaw inVia Reflex Spectrometer System equipped with a frequency doubled Nd:YAG Laser with 100 mW at 532 nm. For all samples, a 20× objective and a grating with 2400 lines mm^{-1} was used and 7 individual scans with 3 accumulations each were averaged. For metal oxide bands, the acquisition time for each accumulation was set to 60 s at 10% laser power in a spectral range of 60−1320 cm^{-1}. For carbonaceous species, the acquisition time was set to 600 s at 0.1% laser power in a range from 1000−2000 cm^{-1}. The data treatment was performed with WiRE 4.2 from Renishaw.

2.3. Catalytic Tests. The catalytic performance of the catalyst samples was determined using an in house built continuous flow laboratory setup. For this purpose 300 mg of the catalyst samples (mesh 300−450 μm) were diluted in SiC (210 μm) and filled into a stainless steel tubular down flow fixed bed reactor (d_i = 7 mm) to obtain a catalyst bed with 35 mm in length. K type thermocouples were placed in front of and behind the catalyst bed and the reactor was heated using a custom made oven (HTM Reetz) regulated with an Eurotherm 2416 temperature controller. The gases were dosed using individual mass flow controllers (Bronkhorst).

The catalyst samples were reduced in situ for 2 h at 500 °C (10 K min^{-1}) in 50% H_2/N_2 (300 mL min^{-1}) before each experiment followed by cooling to the intended starting temperature. The feed gas composition was switched to H_2/CO_2 = 4 in 50% N_2 for the methanation of CO_2 resulting in a weight hourly space velocity (WHSV) of 6000 $mL_{CO_2}\ g_{cat}^{-1}\ h^{-1}$. The gas hourly space velocity (GHSV) with respect to the total gas flow and total volume of the catalyst bed was 13 400 h^{-1}. Gas analysis was performed using an INFICON micro gas chromatograph Fusion (μGC) equipped with molecular sieve (5 Å) and Q BOND columns with Ar or He carriers gas, respectively, and a thermal conductivity detector (TCD). The catalytic activity was recorded in the temperature range of 200−450 °C, increasing the temperature by 50 K per step. Each temperature was kept for ca. 30 min to obtain stable values in the μGC analysis. This procedure was applied at 1 and 10 bar, respectively.

A microchannel packed bed reactor concept with integrated temperature setting possibility (Figure 1) developed at IMVT[45] was utilized for long term stability tests and kinetic measurements. Slit dimensions are 60 × 8 × 1.5 mm^3 (length × width × depth). Compressed air in the range of 100 L min^{-1}, preheated to the reaction temperature with an external device, was used as heat transfer medium in 72 × 36 cross flow microchannels, each 500 μm wide and 230 μm deep. Four axially distributed thermocouples of K type in the metal housing, close to the packed bed, allowed temperature measurement.

The reaction zone was packed with 150 mg (mesh 200−300 μm) of catalyst diluted with SiC (mesh 300−400 μm). The reactants were dosed via MKS mass flow controllers. WHSV values of 80500 $mL_{CO_2}\ g_{cat}^{-1}\ h^{-1}$ were adjusted using the gas composition with the initial amount of 9.1% CO_2, H_2/CO_2 = 4 and the reaction was operated at 6 bar. An industrial catalyst sample with nominal 20 wt % Ni/Al_2O_3 and promoted by an alkaline earth metal was used as standard for comparison in the tests under industrially relevant conditions. As this catalyst was supplied in tablets, it was crushed and sieved to the desired particle size of 200−300 μm.

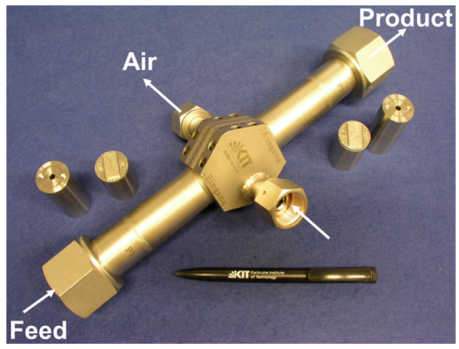

Figure 1. Microchannel reactor with integrated heat management for kinetic measurements of the methanation reaction.

The product composition from the microchannel reactor setup was analyzed using an Agilent online gas chromatograph 7890 including a Pora Plot Q capillary column, a HP Plot 5 Å molecular sieve and He as carrier gas. For detection, thermal conductivity and flame ionization detectors were used.

Conversion and selectivity in the catalytic tests were calculated as follows:

$$\text{conversion: } X(CO_2) = \left(1 - \frac{CO_{2,out}}{CO_{2,out} + CH_{4,out} + CO_{out}}\right)\cdot 100\% \quad (3)$$

When applying higher concentrations in the microchannel reactor, N_2 was used as internal standard for volume correction:

$$\text{conversion: } X'(CO_2) = \left(1 - \frac{CO_{2,out}\cdot N_{2,in}}{N_{2,out}\cdot CO_{2,in}}\right)\cdot 100\% \quad (4)$$

$$\text{yield: } Y(CH_4 \text{ or } CO) = \frac{CH_{4,out} \text{ or } CO_{out}}{CO_{2,out} + CH_{4,out} + CO_{out}}\cdot 100\% \quad (5)$$

$$\text{selectivity: } S(CH_4) = \frac{Y(CH_4)}{X(CO_2)}\cdot 100\% \quad (6)$$

The turnover frequency (TOF) was calculated as moles of CH_4 produced per moles of surface metal atoms per second using the inlet flow of CO_2, the molar gas volume V(m) and the catalyst mass:

$$TOF = \frac{V(CO_2, \text{in})\cdot Y(CH_4)}{V(m)\cdot N(surf)\cdot m(cat)} \quad (7)$$

The number of surface metal atoms N(surf) was estimated using the dispersion from TEM analysis.[44] Hence, all surface metal atoms were assumed to be equally active.

2.4. Kinetic Model. The pseudohomogeneous 1D reactor model was used. The mass balance in differential form was written according to eq 8.

$$\frac{dF_i}{dm_{cat}} = \nu_i R_i \quad (8)$$

Thereby, F_i is the molar flow of the component i [mol s^{-1}], m_{cat} is the catalyst mass [kg], ν_i is the stoichiometric coefficient of the component i, and R_i is the net reaction rate of the component i [mol kg^{-1} s^{-1}]. The inlet boundary condition F_{i0} for each component was calculated according to gas throughput, temperature, pressure, and gas composition adjusted in the experiments. The integration of the literature kinetic models was conducted in MATLAB using a Runge–Kutta (4th order) routine. Kinetic models of Koschany et al.,[46] Kopyscinski et al.,[47] and Zhang et al.[48] were used for comparison with the results of this work.

3. RESULTS AND DISCUSSION

3.1. Catalyst Characterization: Particle Size, Alloy Formation, and Crystal Phases. The desired metal loading was chosen on the basis of literature identifying an optimum of 15–20 wt % of the active metal on the support for the methanation of CO_2 (e.g., refs 49–51) as well as for CO methanation.[31] Elemental analysis of the catalyst samples (Table 1) revealed a total metal loading of about 17 wt % for both catalysts. Therefore, a slightly lower total metal content was obtained for the applied preparation procedure, which means that the metal ions in the solution were not precipitated entirely. The bimetallic catalyst exhibited the intended molar Ni/Fe ratio of 3, which was the most suitable composition for CO_2 methanation reported in literature.[29,33,35] The specific surface area of the catalysts was determined as 220 m^2 g^{-1}. The catalyst samples of the Ni and the bimetallic Ni_3Fe catalyst as well as the pure γ Al_2O_3 support were analyzed by XRD to identify the crystalline phases (Figure 2).

Table 1. Elemental Composition of the Prepared Catalysts Supported on γ Al_2O_3

catalyst	total metal loading [wt %]	Ni [wt %]	Fe [wt %]
Ni	16.6	16.6	-
Ni_3Fe	17.0	12.9	4.1

The XRD patterns of the catalysts are dominated by the reflections of Al_2O_3. The Ni catalyst showed reflections of the Ni(111) plane at 2Θ = 44.5° (ICSD 044767) represented as a shoulder of the reflection from Al_2O_3. At a similar 2Θ value, a reflection of the Fe(110) plane (ICSD 064998) is expected for the iron containing catalyst. The reflections of Ni(111) and Fe(110) could not be resolved by XRD. The shoulder next to the Al_2O_3 reflection appeared to be slightly broader in the case of Ni_3Fe catalyst compared to the monometallic sample. This might be caused by an additional reflection occurring from the Ni_3Fe(111) plane at 2Θ = 44.2° (ICSD 040334).

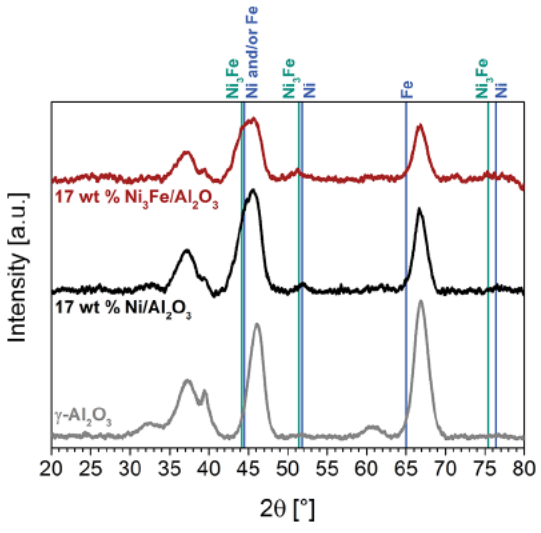

Figure 2. XRD patterns of the reduced 17 wt % Ni/Al_2O_3 (black) and bimetallic 17 wt % Ni_3Fe/Al_2O_3 (red) catalyst samples compared to the pure γ Al_2O_3 support (gray).

An isolated reflection was observed for the Ni(200) plane at 2Θ = 51.8°. Using this reflection a crystallite size of 5.4 nm was estimated from the Scherrer equation. The pattern of the bimetallic catalyst revealed a reflection at slightly lower angles, which can be ascribed to the Ni_3Fe(200) plane at 2Θ = 51.5°. This angular shift based on the formation of a Ni_3Fe alloy and its change in the lattice parameters compared to metallic Ni has been reported in literature.[34,35,52−54] The crystallite size of the alloyed catalyst was calculated as 5.7 nm. No reflections from Fe at 2Θ = 65.0°, Ni_3Fe at 2Θ = 75.8°, or Ni at 2Θ = 76.4° were observed.

The STEM image showed well dispersed metal particles on the support (Figure 3) for the Ni_3Fe catalyst. Small metal nanoparticles with a narrow size distribution (d_p = 3.9 ± 0.9 nm) were observed with a dispersion of 24%. Similar results were obtained for the Ni catalyst regarding both, the metal particle size (d_p = 3.8 ± 0.9 nm) and the dispersion (24%). The sizes of the metal particles from the STEM images are in a similar range as the crystallite sizes estimated from XRD. The particle sizes determined by STEM also accounted for smaller particles that might be invisible for XRD.

Upon iron addition the particle size and, thus, the dispersion remained almost the same (Figure 3). NiFe/alumina catalysts (40 wt %) have been prepared by Hwang et al.[34] via a single step sol–gel method, which led to slightly larger particles of about 7.4 nm (but 2 fold metal loading) as determined by XRD. In contrast, larger metal particles of 10–12 or 13–15 nm depending on the support and loadings were reported in literature for NiFe catalysts that were prepared by impregnation methods.[31,53]

Composition maps of single Ni_3Fe nanoparticles obtained from a STEM EDX spectrum image (Figure 4) revealed that Ni and Fe elements exhibited similar distribution, indicating the formation of alloy particles.

The compositions of the Ni_3Fe nanoparticles quantified by STEM EDX in different regions are shown in Table 2. The calculated Ni/Fe ratios are slightly higher than the overall desired Ni/Fe ratio of 3 and revealed slight local variations.

The Ni_3Fe nanoparticles were further analyzed using HRTEM (Figure 5), and the crystal structure was identified by fast Fourier transformation (FFT) from an individual particle. The lower right part of Figure 5 shows the magnified image of the particle, and the upper right part shows the corresponding FFT, indicating that the catalyst particles consisted of the intended Ni_3Fe alloy, thus, confirming the observations from STEM EDX spectrum imaging and XRD.

Some of the Ni_3Fe particles were surrounded by very small NiO clusters that could not be detected using XRD. This also explains the local variations in the Ni/Fe ratio quantified by STEM EDX. The oxidation of the small Ni particles might have occurred during the TEM sample preparation handled in air. Monometallic iron or iron oxide particles were not observed in the regions explored by electron microscopy.

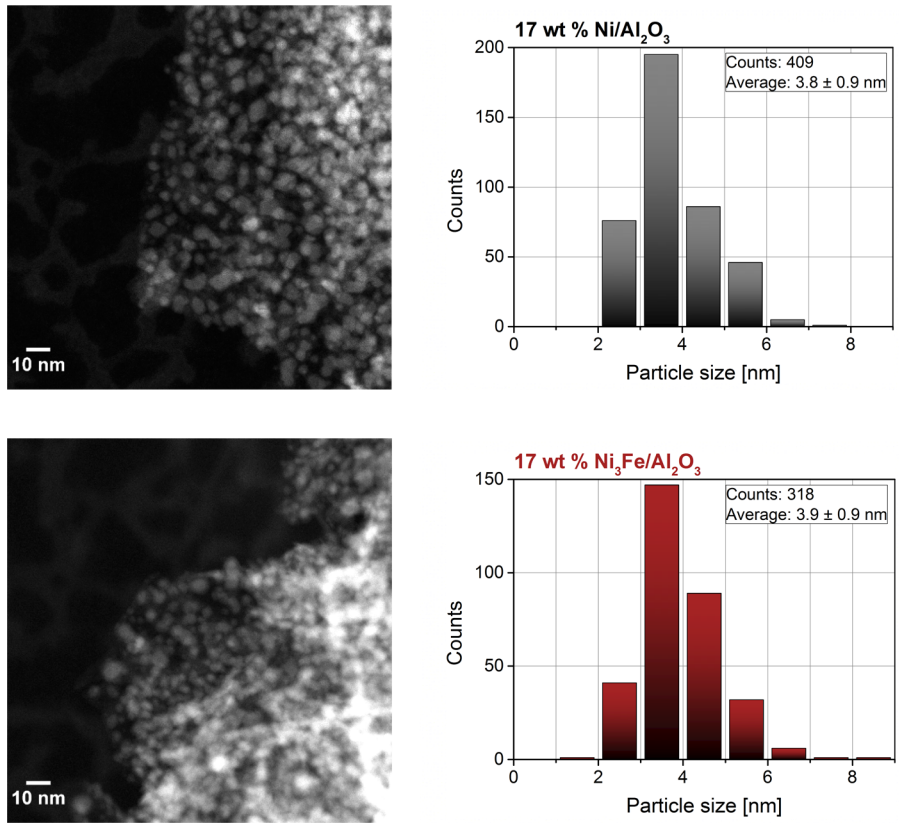

Figure 3. Representative STEM images and particle size distributions of the 17 wt % Ni/Al_2O_3 (upper part) and 17 wt % Ni_3Fe/Al_2O_3 (lower part) catalysts.

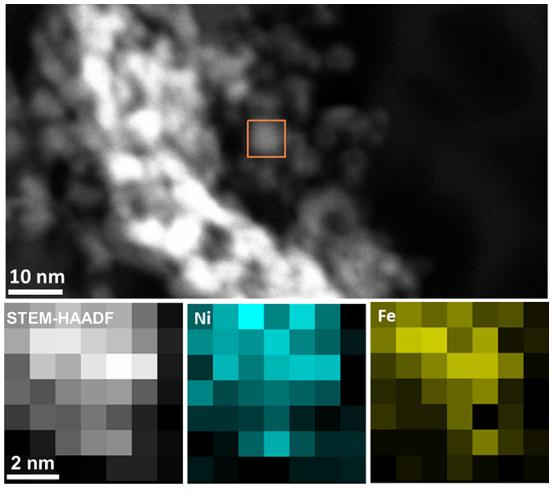

Figure 4. Overview STEM image of the 17 wt % Ni_3Fe/Al_2O_3 catalyst and the corresponding elemental maps obtained from STEM EDX spectrum imaging on an individual particle marked with the box.

Table 2. Quantified Elemental Analysis of the Ni_3Fe Nanoparticles Measured at Different Regions by STEM EDX

	Ni [at %]	Fe [at %]	Ni/Fe ratio
region no. 1	75.5	24.5	3.1
region no. 2	79.7	20.3	3.9
region no. 3	80.6	19.4	4.2
region no. 4	77.6	22.4	3.5
region no. 5	79.6	20.4	3.9

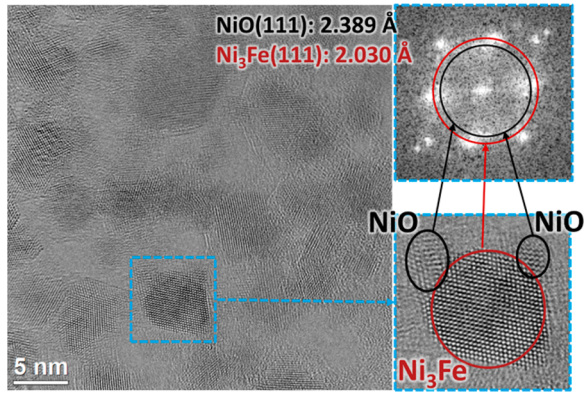

Figure 5. HRTEM image and structure analysis of the 17 wt % Ni_3Fe/Al_2O_3 catalyst by FFT from one particle.

Raman spectroscopy (Figure 6) was performed ex situ on the calcined samples before reduction to gather further structural information on the bimetallic Ni_3Fe alloy catalyst. In addition, a 5 wt % Fe/Al_2O_3 sample and bulk α Fe_2O_3 were used as references to assign the Raman bands. α Fe_2O_3 shows characteristic Raman bands at 222, 244, 290, 404, 492, 605, 617, and 1060 cm^{-1}.[55] These bands were present in the spectrum of the 5 wt % Fe/Al_2O_3 sample. Additionally, two main features appeared at 699 and 750 cm^{-1}, which can both be assigned to $FeAl_2O_4$.[56,57] This does not necessarily imply the presence of bulk $FeAl_2O_4$ but oxidic Fe species in contact with Al_2O_3, as expected for supported nanoparticles. The bimetallic 17 wt % Ni_3Fe/Al_2O_3 alloy catalyst showed also these two features as well as a weak shoulder at 890 cm^{-1}. However, the

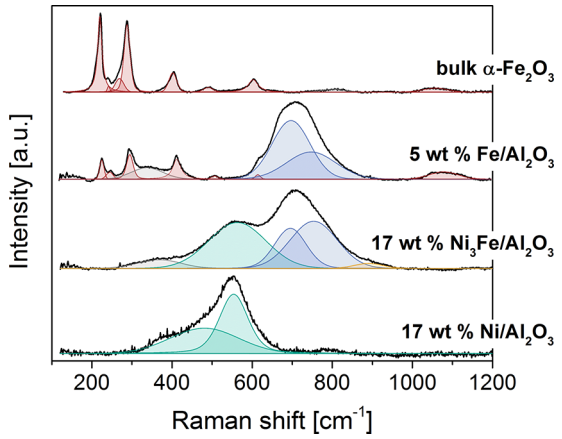

Figure 6. Raman spectra of the calcined 17 wt % Ni_3Fe/Al_2O_3 catalyst and monometallic 17 wt % Ni/Al_2O_3 compared to 5 wt % Fe/Al_2O_3 and bulk α Fe_2O_3. The deconvolution represents in green: Ni−O, blue: A_{1g} vibrations of $FeAl_2O_4$, red: α Fe_2O_3 and orange: shoulder only present for the bimetallic catalyst. A list of the full deconvolution data is given in the Supporting Information.

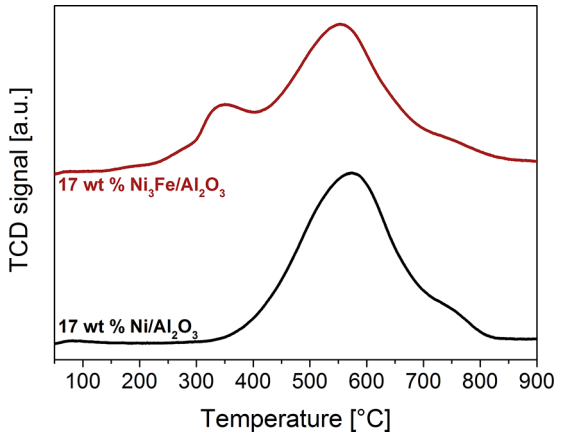

Figure 7. H_2 TPR profiles of the 17 wt % Ni_3Fe/Al_2O_3 (top) and the 17 wt % Ni/Al_2O_3 (bottom) catalyst, conditions: 100 mg of sample, 10% H_2/Ar (50 mL min^{-1}), and a ramp rate of 10 K min^{-1}.

bimetallic catalyst did not show any characteristic bands for Fe_2O_3.[55,58] Since the presence of FeO gives a distinct band at 645 cm^{-1}[55,58] and supported Fe_3O_4 normally gives a main band around 665 cm^{-1},[59] these two iron species were hardly present. The band around 700 cm^{-1} may also originate from $NiFe_2O_4$ spinel in this catalyst. The band at 563 cm^{-1} is a Ni−O stretching mode, which has been shifted to higher wave numbers due to a higher iron content, as it has been observed for oxides of bulk Ni_3Fe.[60,61] The Raman spectrum of 17 wt % Ni/Al_2O_3 shows the band at 554 cm^{-1} with a shoulder around 481 cm^{-1} that can be assigned to Ni−O vibrations, which is in agreement with earlier studies for supported NiO.[62,63]

In general, it is difficult to conclude whether broad Raman signals originate from a superposition of several bands or from a broadening effect due to the small crystallite size of iron oxide species. Raman spectroscopy cannot prove the formation of an alloy, since it is only sensitive to metal−oxygen vibrations and spinels such as $NiFe_2O_4$ and $FeAl_2O_4$ give similar main bands. However, the slight change of the broad Fe−O vibration band might indicate a different crystal structure compared to pure supported iron oxide and a strong interaction between Fe^{3+} and Ni^{2+}already in this "precursor" state.

The reducibility of the Ni_3Fe catalyst was investigated by temperature programmed reduction with H_2 (H_2 TPR, Figure 7) and compared to the profile of the monometallic Ni catalyst. The H_2 consumption profile of the Ni catalyst revealed one main peak at 573 °C referring to the reduction of NiO to metallic Ni. The shoulder around 750 °C could be ascribed to smaller NiO particles exhibiting stronger interactions with the support, which have also been observed in HRTEM images. Other possible species such as $NiAl_2O_4$ that would reduce at higher temperatures (>800 °C, e.g., refs 51,64) have not been detected. The results from TPR confirmed the presence of small Ni particles with a uniform size eliminating the possible formation of larger agglomerates on the catalyst, which would result in reduction peaks at lower temperatures.

The TPR profile of the Ni_3Fe catalyst showed the main peak at 555 °C and an additional peak at 350 °C. Two reduction peaks have also been reported in other studies and can be assigned to the reduction of Fe_2O_3 to Fe_3O_4 in the ternary NiFe oxide (350 °C) and to the reduction of Fe_3O_4 to Fe and NiO to Ni (555 °C).[34,37,65] Other studies involving bimetallic NiFe catalysts with higher metal loading and larger metal particles on a support with lower specific surface area showed TPR profiles with one single broad reduction peak. A second reduction peak appeared for catalysts with a higher amount of Fe.[32,66] In our case, the high temperature reduction peak might be sharper due to the small metal particles compared to literature and, therefore, separated into two peaks. The main reduction peak of the Ni_3Fe catalyst in Figure 7 shifted to slightly lower temperatures (573 to 555 °C), as a consequence of a higher reducibility of the Ni_3Fe alloy compared to the monometallic Ni catalyst.[32,34]

The combined characterization results from XRD, STEM, Raman spectroscopy and H_2 TPR led to the conclusion that a high amount of the desired Ni_3Fe alloy was formed and small, rather uniformly sized particles were present. In addition, some very small Ni/NiO particles were identified but no Fe containing single metal particles were observed. Hence, the supported Ni and Ni_3Fe catalysts exhibited similar structural properties such as total metal content, metal particle size and dispersion, which is optimal to determine the potential of the Ni_3Fe alloy catalyst in the methanation of CO_2 and to gain insight into structure−performance relationships.

3.2. Catalytic Performance: Screening of Temperature and Pressure. The catalytic performance of both catalysts was investigated in the temperature range of 200−450 °C during the methanation of CO_2 at atmospheric pressure (1 bar) and at elevated pressure (10 bar) using a tubular packed bed reactor. Figure 8 shows the catalytic data for the Ni_3Fe alloy catalyst compared to the monometallic Ni catalyst. At 200 °C and 1 bar, the conversion of CO_2 (Figure 8a) was very low for both catalysts (2−3%). The conversion started between 200−250 °C and increased with rising temperature. At 250−300 °C, a slightly higher conversion of CO_2 was achieved for the Ni_3Fe catalyst (21−76%) compared to the monometallic Ni catalyst (15−73%). The best results for both catalysts at atmospheric pressure were realized at 350 °C (Ni_3Fe: 82%; Ni: 85%). A further increase of the temperature resulted in a decline of the activity due to the thermodynamic equilibrium,[16] converting only 71% (Ni_3Fe) and 72% (Ni) of CO_2 at 450 °C.

Increaseing the pressure to 10 bar resulted in a significantly higher conversion of CO_2 in the temperature range of 250−450 °C. The superior activity of the alloyed catalyst emerged already at 250 °C, where an exceptional CO_2 conversion of 87% (21%

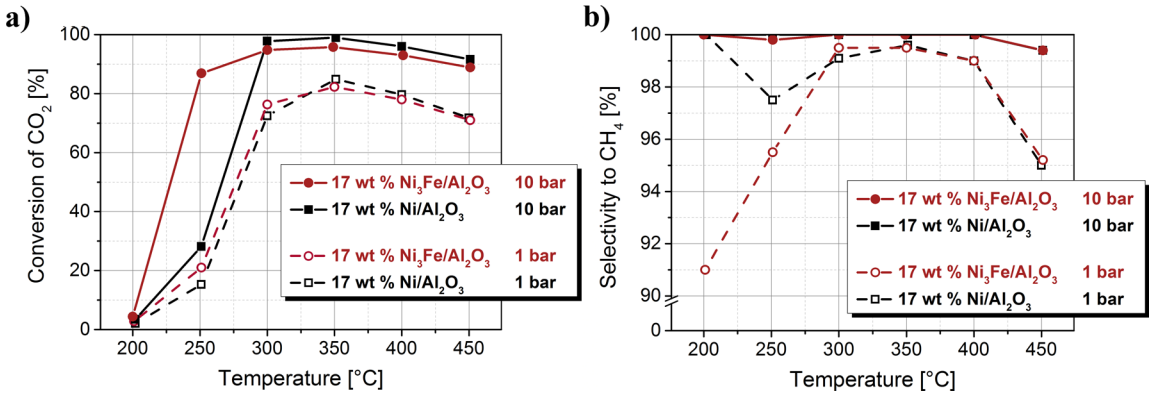

Figure 8. (a) CO_2 conversion and (b) CH_4 selectivity of the 17 wt % Ni/Al_2O_3 (squares, black) and 17 wt % Ni_3Fe/Al_2O_3 (circles, red) catalysts in the methanation of CO_2 at 1 bar (open symbols) and 10 bar (filled symbols) (6000 $mL_{CO_2}\ g_{cat}^{-1}\ h^{-1}$).

at 1 bar) was observed, whereas the Ni catalyst reached moderate activity with a conversion of only 28% (15% at 1 bar). For the Ni catalyst, a similar steep increase in activity occurred at 300 °C at the higher pressure, following the trend observed at atmospheric pressure. Both catalysts achieved excellent activity at 300−350 °C, converting 98−99% (Ni) and 95−96% (Ni_3Fe) of the CO_2 fed into the reactor.

The selectivity toward CH_4 is plotted in Figure 8b. As the reaction started at 250 °C under atmospheric pressure the Ni_3Fe catalyst showed moderate selectivity to CH_4 (ca. 96%). The value reached by the monometallic Ni catalyst was slightly higher (98%). CO was formed as the only byproduct for both catalysts. The selectivity to CH_4 increased with temperature and reached values >99% at 300−350 °C for both catalysts. At higher temperatures, the selectivity decreased slightly, which was caused by the formation of CO due to the endothermic reverse water−gas shift reaction (eq 2).[16] At 10 bar, both catalysts produced CH_4 with a selectivity close to 100% over the whole temperature range. Only at 450 °C, the selectivity toward CH_4 declined slightly due to the detection of ca. 600 ppm of CO in the μGC.

The significantly enhanced low temperature activity over the Ni_3Fe alloy catalyst compared to the monometallic Ni reference especially at elevated pressure (10 bar) supports results by Hwang et al.[34] or Ren et al.[36] However, in those studies, substantially different reaction conditions, catalyst loadings, and support materials were used, which makes a direct comparison difficult. At higher temperatures, no significant promoting influence of Fe was observed.

3.3. Long-Term Performance and Kinetic Data. The catalytic results in section 3.2 showed that the Ni_3Fe alloy catalyst is an attractive alternative compared to a monometallic Ni catalyst. For a more realistic performance rating the Ni_3Fe catalyst was compared with a commercially available Ni based methanation catalyst under industrially oriented reaction conditions with focus on catalyst stability and avoidance of mass and heat transport limitations using a microchannel packed bed reactor.

The extent of the external mass transport limitation was examined using the Carberry number.[67] The inequality was clearly fulfilled with $6 \times 10^{-3} < 0.1$ at given experimental conditions. The mass transfer coefficient was taken from ref 68. The reaction rate was approximated with the literature kinetics given by Koschany et al.[46] with an apparent reaction order of 0.5; this approximation was also applied for the evaluation of the internal mass transport limitation, i.e. the Weisz−Prater criterion.[69] On the average sized particle of 250 μm, the Weisz number was calculated to 0.07 and satisfied the suggested limit of 0.08 (360 °C, 6 bar, 9% CO_2, H_2/CO_2 = 4). The effective diffusion coefficient for CO_2 was governed by Knudsen regime to be $1.1 \times 10^{-6}\ m^2\ s^{-1}$ (particle porosity of 0.7 and tortuosity of 3). The extent of the external heat transfer limitation was evaluated according to Mears.[67] The heat transfer coefficient from particle to fluid in the packed bed was calculated to 1488 $W\ m^{-2}\ K^{-1}$ from[70] at 360 °C and a Reynolds particle number of 24 (Pr = 0.7) for the examined reaction mixture and conditions. The film overheating on the 250 μm particle was calculated to 2.7 K which is slightly above the suggested limit of 2 K, however, this was considered negligible for the determination of the kinetic parameters.

The long term stability of the commercial Ni based methanation catalyst is shown in Figure 9a in terms of CO_2 conversion as a function of time on stream (TOS). The corresponding selectivity toward CH_4 is depicted in Figure 9b. Starting at 358 °C, the commercial Ni based catalyst achieved a CO_2 conversion of 52% with a selectivity toward CH_4 of 90%. CO was detected as the only byproduct. These conditions were kept for a 47 h TOS steady state operation during which a linear decline in conversion of $-0.12\%\ h^{-1}$ was observed. After 47 h, the conversion of CO_2 decreased to 46%, although the selectivity toward CH_4 remained constant (90−91%).

The effectiveness factor is used to describe the percentage of pore utilization of the catalysts and is estimated to around 90% according to ref 71. Thus, the temperature was decreased to minimize mass transport limitations. At 328 °C, 22% of CO_2 was converted by the catalyst with a calculated effectiveness factor of >95%, and therefore, the catalyst particles in the bed operated near full utilization. The selectivity toward CH_4 decreased slightly to 85% due to an increasing production of CO. As the formation of CO by the reverse water−gas shift reaction is generally assumed to happen at higher temperature, this increased CO production could indicate that the parallel reverse water−gas shift reaction can improve in importance due to the competition on the same active sites. However, the selectivity calculation could also be falsified by the overall lower concentration of products at lower conversion (i.e., leading to a higher experimental error).

The temperature was kept constant at 328 °C for 44 h, during which a further slight decline of the CO_2 conversion of $-0.09\%\ h^{-1}$ was observed following the trend monitored at 358 °C and resulting in 18% CO_2 conversion in the end. Additionally, a declining selectivity toward CH_4 to 81% was

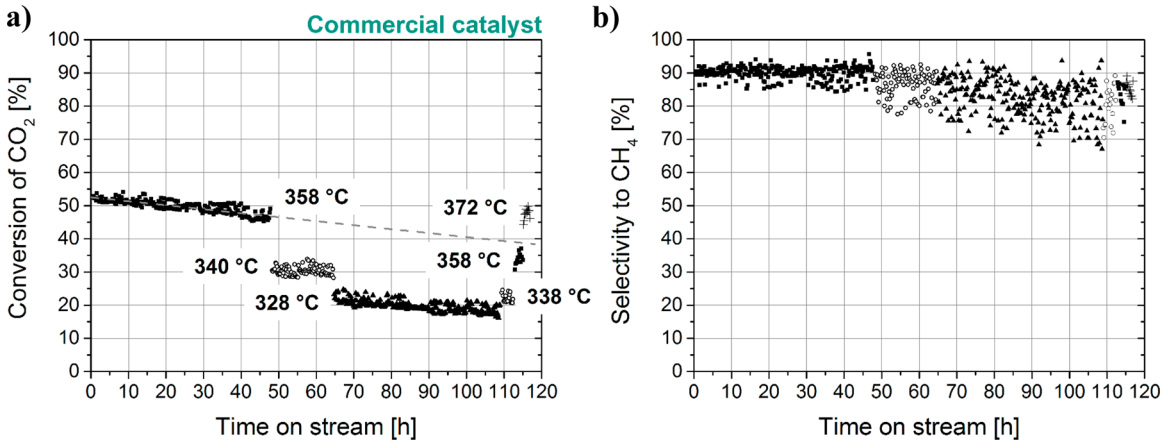

Figure 9. (a) Conversion of CO_2 and (b) selectivity toward CH_4 of the commercial Ni based methanation catalyst during long term performance testing at 80 500 $mL_{CO_2}\ g_{cat}^{-1}\ h^{-1}$ and 6 bar.

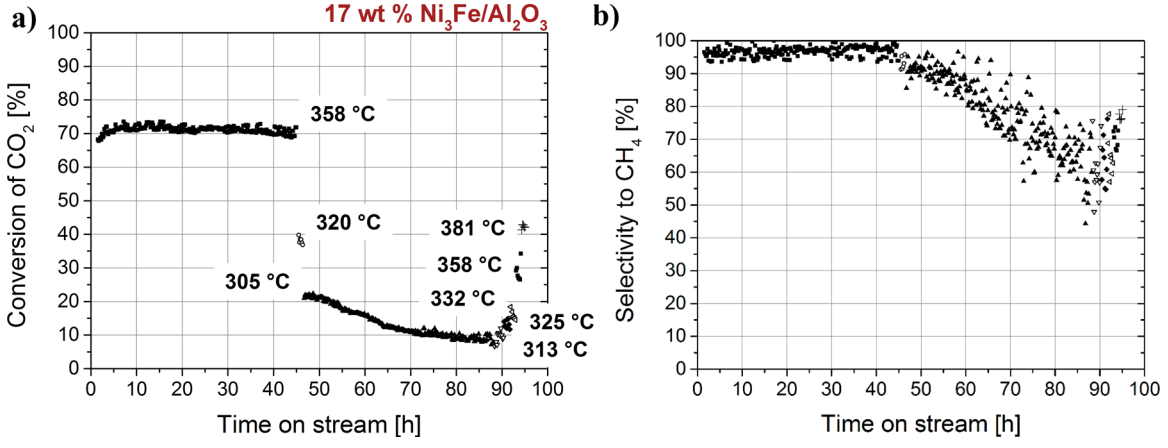

Figure 10. (a) Conversion of CO_2 and (b) selectivity toward CH_4 of the 17 wt % Ni_3Fe/Al_2O_3 catalyst during long term performance testing at 80 500 $mL_{CO_2}\ g_{cat}^{-1}\ h^{-1}$ and 6 bar.

observed over 44 h TOS at 328 °C. Increasing the temperature to 358 °C again led to a conversion of 34%, which is nearly the value that would have been expected for a linear decrease over time at this temperature.

The conversion of CO_2 achieved by the Ni_3Fe system is shown in Figure 10a as a function of TOS, the corresponding selectivity toward CH_4 is depicted in Figure 10b. At 358 °C, the Ni_3Fe catalyst achieved a high CO_2 conversion of 71%, which was superior to the conversion reached by the commercial catalyst at the same starting temperature. In addition, excellent stability was achieved over 45 h, which is of crucial importance for industrial applications. A linear decline in the conversion of −0.02% h^{-1} was observed, which was 6 times slower than for the commercial catalyst. During this period, the selectivity toward CH_4 was high with a constant value of around 98% making the bimetallic Ni_3Fe system superior to the commercial Ni catalyst ($S(CH_4)$ = 91−92%). The effectiveness factor for this condition was estimated to 70%. In accordance with the long term performance test of the commercial methanation catalyst, the temperature was then decreased to obtain similar CO_2 conversions and an effectiveness factor of >95% at about 305 °C (compared to 328 °C for the commercial catalyst). At that temperature, 21% of CO_2 was converted for the first 6 h of TOS. The selectivity toward CH_4 slightly decreased to 91% due to the lower temperature, which is also in alignment with the results from the commercial catalyst. The initial turnover frequency (TOF) of the Ni_3Fe catalyst based on the yield of CH_4 and the catalyst characterization data was calculated to be 0.26 s^{-1} (305 °C, 6 bar). The received TOF value located in typical dimensions for alumina supported Ni catalysts reported in literature, ranging from 0.041−0.097 s^{-1}[72] and 0.1 s^{-1}[73] up to 0.69 s^{-1}.[74] However, the reaction rates are difficult to compare due to the unknown effectiveness factors and various reaction conditions, which were applied in different studies. This is also the case, if results of long term performance tests in the literature are compared.

After 6 h TOS with near constant conversion at 305 °C, the conversion of Ni_3Fe dropped significantly during the total 40 h TOS period at 305 °C to only 9% in the end. The degradation was ca. 17 times faster than at 358 °C. The deactivation behavior in this period was less predictable due to a nonlinear conversion decline. At the same time, the selectivity toward CH_4 declined distinctly to only 63% after 40 h TOS due to the rising production of CO. Both catalyst deactivation and loss of selectivity were considerably less pronounced for the commercial system under full pore utilization and lower temperature conditions compared to the Ni_3Fe catalyst. Therefore, the low temperature leading to a higher CO production ability could probably accelerate the degradation process due to an enhanced probability for soot formation from CO or segregation of the particles. Slightly decreasing conversion of CO_2 over time has also been reported in

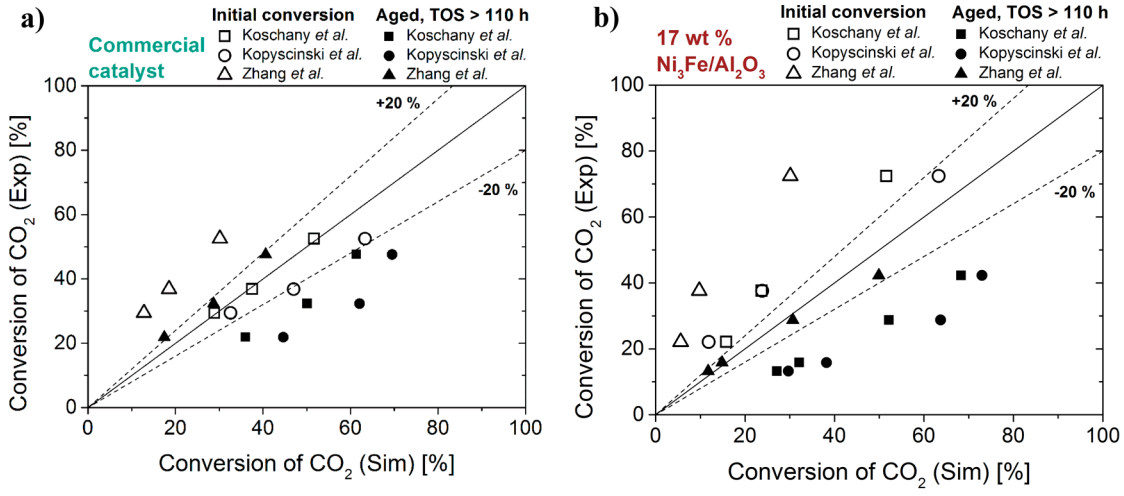

Figure 11. Conversions of CO_2 for the (a) commercial Ni catalyst and (b) the 17 wt % Ni_3Fe/Al_2O_3 catalyst directly compared with kinetic models from literature by Koschany et al.,[46] Kopyscinski et al.,[47] and Zhang et al.[48] under methanation conditions (WHSV = const.) at different temperatures.

literature and seems to be a common problem for Ni catalysts.[75−79] Such deactivation over time was attributed to both sintering of the metal particles and a small degree of coke formation,[75,78,79] but also oxidation of Ni during long term operation might play a role.[15,41,75,80] Studies on degradation under CO methanation conditions revealed that asymptotic conversion decline is a common problem[48,81] and could be attributed to a strong deactivation mechanism (e.g., pore mouth blockage by coke).[82] Indeed, in most cases, carbon deposition due to CO decomposition to surface carbon was speculated as the main deactivation route.[81,83−86]

After 40 h of TOS at 305 °C the temperature was increased gradually resulting in an improved conversion and selectivity. However, even at the initial temperature of 358 °C only 29% of CO_2 (compared to 71% at the beginning) was converted with a selectivity of 70% toward CH_4 (compared to 98% in the beginning). Hence, a serious deactivation of the Ni_3Fe catalyst system occurred during the low temperature period.

Comparison of both catalyst systems revealed an enhanced conversion, selectivity, and stability for the Ni_3Fe system at 358 °C pointing to a synergetic effect of Ni and Fe. The enhanced activity may be explained by parallel contributions of an enhanced CO_2 adsorption and activation at the Fe species[35,36] and an optimal CO dissociation energy of the NiFe alloy that has been claimed in DFT studies[29] and confirmed exper imentally.[31,33,34] However, the Ni_3Fe catalyst was not able to further convert CO to methane at 305 °C due to a combination of low temperature and consequently increased CO formation ability. Similar behavior was observed in the screening experiment (Figure 8) at 250 °C and 1 bar. Increased CO formation was also observed for iron rich NiFe catalysts.[35] Furthermore, Fe catalysts are active in the reverse water−gas shift reaction (eq 2) applied in Fischer−Tropsch processes.[87,88] Hence, operando spectroscopic investigations[4,89−93] should be conducted in the future to elucidate the structure of the Ni_3Fe catalyst at work and to evaluate whether surface segregation of Fe might play a role in the enhanced CO production. However, this is beyond the scope of this study, and such studies are currently being performed on these well characterized Ni based catalysts.

Due to the deactivation that occurs at lower temperatures, the methanation of CO_2 with the Ni_3Fe catalyst needs to be operated at 358 °C to maintain optimal performance. Since internal mass transport limitations could only be prevented at different temperatures (305 °C for Ni_3Fe, 328 °C for the commercial catalyst), a more pronounced deactivation of the commercial catalyst at 305 °C in alignment with the deactivation observed on the Ni_3Fe catalyst due to further increased CO formation also on the pure Ni catalyst could not be ruled out.

In the following, the measured kinetic data of the 17 wt % Ni_3Fe/Al_2O_3 and the commercial catalyst were compared with literature models by Koschany et al.,[46] Kopyscinsky et al.,[47] and Zhang et al.[48] (Figure 11) developed for Ni/Al_2O_3 catalysts. The activity of the commercial catalyst in its fresh state was extrapolated based on data points at TOS < 70 h and was compared to literature models (initial conversion) in Figure 11a. Excellent agreement of the experimental conversion was found with the model given by Koschany et al.[46] and a relatively accurate prediction was made by the model of Kopyscinsky et al.[47] The kinetics by Zhang et al.[48] were less accurate while overestimating the experimental conversion by a factor of ≈2. Furthermore, the experimental conversion data for 358 °C at TOS ∼ 110 h from Figures 8 and 9 were averaged and plotted for comparison in the same graph (marked as "aged"). It was observed that still tolerable agreement was achieved by the Koschany model, whereas the error by the Kopyscinski model increased up to ca. 40%. Based on this information, the development of the time dependent deactivation description for the commercial catalyst is feasible, which could play a role in technical applications. The amount of CO produced as byproduct could not be neglected. Therefore, despite great accuracy, the model of Koschany et al.[46] needs to be corrected as it ignores the formation of CO species in the reaction.

The Ni_3Fe catalyst showed CO_2 conversions in the same order of magnitude as predicted by the literature kinetic models (Figure 11b). Due to the decline of the performance at lower temperatures, two regions were determined for kinetic comparison. The first experimental conversion data are taken from the period of 40−50 h TOS under extremely low activity loss of the catalyst (i.e., for 320/358 °C, almost initial

conversion). According to Figure 11b, the obtained activity of the fresh 17 wt % Ni_3Fe/Al_2O_3 catalyst was clearly higher than that of pure Ni/Al_2O_3 systems from literature,[46−48] emphasizing the synergetic effect of Ni and Fe. As a result, higher conversions were obtained in this work with a significantly lower Ni loading (17 wt %) in the Ni_3Fe catalyst compared to the 50 wt % Ni catalysts utilized by Kopyscinski et al.[47] and Zhang et al.,[48] which makes the bimetallic Ni_3Fe system very attractive from the economical point of view. The best match of the kinetic data in this region was obtained with the model given by Koschany et al.[46] and Kopyscinski et al.,[47] which underestimated the conversion only up to 30%. The model of Zhang et al.[48] underestimated the kinetic measurements of this work by a factor of ≈2 and was considered less appropriate for this regime.

The "aged" conversion data points were taken after the low temperature period (40−90 h TOS), which led to a subsequent CO_2 conversion decrease by a factor of ≈2 (i.e., in 90−95 h of TOS). The model of Zhang et al.[48] revealed the best accuracy with ±20%, whereas the others overestimated the experimental data considerably by around 40%. Obviously, a rough estimation of the catalyst activity by the kinetic models is possible as a precise determination of the kinetic parameters is aggravated by the deactivation process.

Although, the comparison of the calculated and the measured CO_2 conversions seemed promising using almost all models, the description of the selectivities toward CH_4 and CO remains open. The reason for this is the continuous decline of the selectivity toward CH_4 with progression of deactivation at lower temperatures without reaching a steady state even after 45 h TOS. A simple time dependent extrapolation in activity and selectivity is not possible for the Ni_3Fe catalyst in the lower temperature regime. The high amount of CO produced at 305 °C could not be reflected by any model. From this viewpoint, the model given by Koschany et al.[46] was found as the most inappropriate due to a complete negligence of the CO species in the reaction system. The models by Kopyscinski et al.[47] and Zhang et al.[48] predicted selectivities toward CO at lower temperatures of around 3 and 10%, respectively; among them the model by Zhang reflected the CO trend best. The kinetics by Kopyscinski et al.[47] and Zhang et al.[48] are thus considered as potential candidates for parameter estimation.

3.4. Characterization of the Catalysts after Long-Term Application. Since both catalyst systems suffered from deactivation in the long term experiments they were characterized afterwards to gain information on the deactivation mechanism. Raman spectroscopy (Figure 12) revealed the deposition of carbon species on both catalysts.

The Raman bands around 1380 and 1595 cm^{-1} could be assigned to the D1 and G bands representing a disordered graphitic structure and an ideal graphitic lattice, respectively.[94,95] The absence of further defect bands as well as the distinct and narrow shape of the D1 and G bands with full widths at half maximum of around 50 and 70 cm^{-1}, respectively, indicated that the carbon depositions were graphitic rather than amorphous. In case of the Ni_3Fe system, the carbon formation might have occurred during the low temperature period where CO was formed that caused carbon deposits on Ni based catalysts during CO methanation.[81,84,85] Even though Raman microscopic measurements are barely quantitative, the intensity of the carbon signals was so low (compared to similar measurements on carbon poisoned Ni

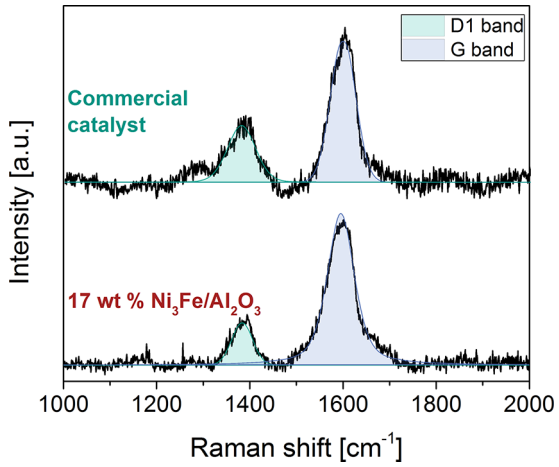

Figure 12. Raman spectroscopy performed ex situ on the 17 wt % Ni_3Fe/Al_2O_3 and the commercial Ni based catalyst after the long term experiment under industry oriented conditions.

based catalysts within our group) that the actual deposition might be very subtle.

Another reason for the deactivation of the catalysts might be sintering of the metal particles. Therefore, STEM images of the spent Ni_3Fe catalyst were recorded after re reduction. The evaluation of the average particle size (Figure 13) showed a

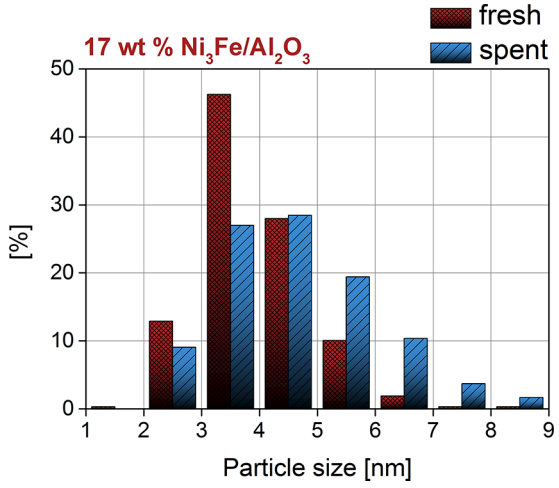

Figure 13. STEM evaluation of the 17 wt % Ni_3Fe/Al_2O_3 catalyst in the fresh state (red) and after the long term experiment (blue).

slight increase from 3.9 ± 0.9 nm to 4.6 ± 1.3 nm. Especially particles in the range of 5−7 nm were observed to a higher extent on the spent catalyst. The dispersion decreased to 19% for the spent catalyst (fresh: 24%). HRTEM and STEM EDX evaluation of the spent catalyst (cf. Supporting Information, Figures S1−S3 and Table S4) showed that still most of the Ni and Fe were alloyed with similar Ni/Fe ratios compared to the fresh catalyst. Moreover, the additional reduction step to recover a full reduction of the used catalyst might have contributed to redispersion effects.[96]

The characterization results of the spent Ni_3Fe catalyst indicated that the loss of activity in the present case seemed to be caused by a loss of metal particle dispersion combined with some carbon deposition (cf. discussion with respect to the long term experiments). In addition, some oxidation of the active sites might also be responsible for the deactivation. Carbon

formation, particle sintering, and loss of metal dispersion might have occurred at all temperatures on the commercial catalysts, explaining the slightly diminishing CO_2 conversion independent of the temperature. Because of the high performance stability of the Ni_3Fe catalyst, we suggest that carbon deposition for this catalyst occurred only during the low temperature sequence when more CO was formed, and therefore, the initial activity could not be retrieved after increasing the temperature again. Slight particle growth and loss of metal dispersion might be the reason for the minimal loss of activity during the first 45 h of TOS.

4. CONCLUSIONS

A promising 17 wt % Ni_3Fe alloy catalyst supported on γ Al_2O_3 with high dispersion was prepared (24%) by a homogeneous deposition−precipitation method with urea. The combination of all results obtained from extensive characterization verified that a high fraction of Ni and Fe formed the intended Ni_3Fe alloy as 4 nm particles with a narrow size distribution. Catalytic tests revealed an enhanced low temperature activity of Ni_3Fe compared to a Ni monometallic reference catalyst, which was most prominent at elevated pressure. Long term experiments of 45 h under industrially oriented conditions including much higher catalyst load revealed a significantly enhanced activity (71% conversion of CO_2) and selectivity (>98% selectivity toward CH_4) of the Ni_3Fe alloy compared to a commercially available Ni based methanation catalyst. Most remarkably, the 17 wt % Ni_3Fe/Al_2O_3 catalyst was highly stable above 350 °C, whereas a decline of conversion was observed for the commercial catalyst. Deactivation of the Ni_3Fe system occurred in the low temperature regime and the selectivity shifted significantly toward CO. Both catalysts showed some carbon deposition after the long term treatment, which may contribute to the deactivation phenomena. Comparison of kinetic measurements with literature models for Ni/Al_2O_3 catalysts supported the higher catalytic performance of the Ni_3Fe system, emphasizing the synergetic effect of Ni and Fe. In conclusion, an outstanding catalyst with high performance and stability was obtained when combining Ni and Fe in the mid temperature (358 °C) methanation of CO_2 for power to gas application.

■ ASSOCIATED CONTENT

Supporting Information

The Supporting Information is available free of charge on the ACS Publications website at DOI: 10.1021/acscatal.7b01896.

Details about catalyst characterization by Raman spectroscopy, curve fitting parameters; estimation of transport limitations, effectiveness factors and experimental data, STEM image, STEM EDX results, and HRTEM image with FFT of the spent 17 wt % Ni_3Fe/Al_2O_3 catalyst after the long term performance test; EDX results of the Ni_3Fe nanoparticles on the spent catalyst (PDF)

AUTHOR INFORMATION

Corresponding Authors

*E mail: wolfgang.kleist@rub.de. Phone: +49 234 32 24121.
*E mail: grunwaldt@kit.edu. Phone: +49 721 608 42120.

ORCID

Wolfgang Kleist: 0000 0002 9364 9946
Jan-Dierk Grunwaldt: 0000 0003 3606 0956

Present Address

#Laboratory of Industrial Chemistry, Ruhr University Bochum, D 44801 Bochum, Germany

Notes

The authors declare no competing financial interest.

ACKNOWLEDGMENTS

This work was funded and supported by KIT and the Helmholtz Reseach School "Energy Related Catalysis". The authors thank Dr. Thomas Bergfeld (IAM AMP, chemical analytics) and Angela Beilmann (BET, H_2 TPR). Special thanks go to KIT and DFG for financing the Raman spectrometer (INST 121384/73 1).

REFERENCES

(1) Schlögl, R. *ChemSusChem* **2010**, *3*, 209−222.
(2) Schüth, F. *Chem. Ing. Tech.* **2011**, *83*, 1984−1993.
(3) Centi, G.; Perathoner, S. *Greenhouse Gases: Sci. Technol.* **2011**, *1*, 21−35.
(4) Kalz, K. F.; Kraehnert, R.; Dvoyashkin, M.; Dittmeyer, R.; Gläser, R.; Krewer, U.; Reuter, K.; Grunwaldt, J. D. *ChemCatChem* **2017**, *9*, 17−29.
(5) Thomas, J. M. *ChemSusChem* **2014**, *7*, 1801−1832.
(6) Zhao, H.; Wu, Q.; Hu, S.; Xu, H.; Rasmussen, C. N. *Appl. Energy* **2015**, *137*, 545−553.
(7) Hashimoto, K.; Yamasaki, M.; Fujimura, K.; Matsui, T.; Izumiya, K.; Komori, M.; El Moneim, A. A.; Akiyama, E.; Habazaki, H.; Kumagai, N.; Kawashima, A.; Asami, K. *Mater. Sci. Eng., A* **1999**, *267*, 200−206.
(8) Stemer, M. *Erneuerbare Energien und Energieeffizienz Renewable Energies and Energy Efficiency*; Kassel University Press GmbH: Kassel, Germany, 2009; Vol. *14*.
(9) Kopyscinski, J.; Schildhauer, T. J.; Biollaz, S. M. A. *Fuel* **2010**, *89*, 1763−1783.
(10) Götz, M.; Lefebvre, J.; Mörs, F.; McDaniel Koch, A.; Graf, F.; Bajohr, S.; Reimert, R.; Kolb, T. *Renewable Energy* **2016**, *85*, 1371−1390.
(11) Rönsch, S.; Schneider, J.; Matthischke, S.; Schlüter, M.; Götz, M.; Lefebvre, J.; Prabhakaran, P.; Bajohr, S. *Fuel* **2016**, *166*, 276−296.
(12) Wang, W.; Wang, S.; Ma, X.; Gong, J. *Chem. Soc. Rev.* **2011**, *40*, 3703−3727.
(13) Gao, J.; Liu, Q.; Gu, F.; Liu, B.; Zhong, Z.; Su, F. *RSC Adv.* **2015**, *5*, 22759−22776.
(14) Aziz, M. A. A.; Jalil, A. A.; Triwahyono, S.; Ahmad, A. *Green Chem.* **2015**, *17*, 2647−2663.
(15) Mutz, B.; Carvalho, H. W. P.; Mangold, S.; Kleist, W.; Grunwaldt, J. D. *J. Catal.* **2015**, *327*, 48−53.
(16) Gao, J.; Wang, Y.; Ping, Y.; Hu, D.; Xu, G.; Gu, F.; Su, F. *RSC Adv.* **2012**, *2*, 2358−2368.
(17) Türks, D.; Mena, H.; Armbruster, U.; Martin, A. *Catalysts* **2017**, *7*, 152.
(18) Brooks, K. P.; Hu, J.; Zhu, H.; Kee, R. J. *Chem. Eng. Sci.* **2007**, *62*, 1161−1170.
(19) Liu, Z.; Chu, B.; Zhai, X.; Jin, Y.; Cheng, Y. *Fuel* **2012**, *95*, 599−605.
(20) Belimov, M.; Metzger, D.; Pfeifer, P. *AIChE J.* **2017**, *63*, 120−129.
(21) Bette, N.; Thielemann, J.; Schreiner, M.; Mertens, F. *ChemCatChem* **2016**, *8*, 2903−2906.
(22) Yan, Y.; Dai, Y.; He, H.; Yu, Y.; Yang, Y. *Appl. Catal., B* **2016**, *196*, 108−116.
(23) Liu, J.; Bing, W.; Xue, X.; Wang, F.; Wang, B.; He, S.; Zhang, Y.; Wei, M. *Catal. Sci. Technol.* **2016**, *6*, 3976−3983.
(24) Guo, M.; Lu, G. *Catal. Commun.* **2014**, *54*, 55−60.
(25) Li, Y.; Lu, G.; Ma, J. *RSC Adv.* **2014**, *4*, 17420−17428.
(26) Zhen, W.; Li, B.; Lu, G.; Ma, J. *RSC Adv.* **2014**, *4*, 16472−16479.

(27) Lange, F.; Armbruster, U.; Martin, A. *Energy Technol.* **2015**, *3*, 55−62.
(28) Mihet, M.; Lazar, M. D. *Catal. Today* **2016**, DOI: 10.1016/j.cattod.2016.12.001.
(29) Andersson, M. P.; Bligaard, T.; Kustov, A.; Larsen, K. E.; Greeley, J.; Johannessen, T.; Christensen, C. H.; Nørskov, J. K. *J. Catal.* **2006**, *239*, 501−506.
(30) Bligaard, T.; Nørskov, J. K.; Dahl, S.; Matthiesen, J.; Christensen, C. H.; Sehested, J. *J. Catal.* **2004**, *224*, 206−217.
(31) Kustov, A. L.; Frey, A. M.; Larsen, K. E.; Johannessen, T.; Nørskov, J. K.; Christensen, C. H. *Appl. Catal., A* **2007**, *320*, 98−104.
(32) Tian, D.; Liu, Z.; Li, D.; Shi, H.; Pan, W.; Cheng, Y. *Fuel* **2013**, *104*, 224−229.
(33) Sehested, J.; Larsen, K.; Kustov, A.; Frey, A.; Johannessen, T.; Bligaard, T.; Andersson, M.; Nørskov, J.; Christensen, C. *Top. Catal.* **2007**, *45*, 9−13.
(34) Hwang, S.; Hong, U. G.; Lee, J.; Baik, J. H.; Koh, D. J.; Lim, H.; Song, I. K. *Catal. Lett.* **2012**, *142*, 860−868.
(35) Pandey, D.; Deo, G. *J. Mol. Catal. A: Chem.* **2014**, *382*, 23−30.
(36) Ren, J.; Qin, X.; Yang, J. Z.; Qin, Z. F.; Guo, H. L.; Lin, J. Y.; Li, Z. *Fuel Process. Technol.* **2015**, *137*, 204−211.
(37) Kang, S. H.; Ryu, J. H.; Kim, J. H.; Seo, S. J.; Yoo, Y. D.; Sai Prasad, P. S.; Lim, H. J.; Byun, C. D. *Korean J. Chem. Eng.* **2011**, *28*, 2282−2286.
(38) Burattin, P.; Che, M.; Louis, C. *J. Phys. Chem. B* **1999**, *103*, 6171−6178.
(39) Bitter, J. H.; van der Lee, M. K.; Slotboom, A. G. T.; van Dillen, A. J.; de Jong, K. P. *Catal. Lett.* **2003**, *89*, 139−142.
(40) Geus, J. W.; van Dillen, A. J. Preparation of Supported Catalysts by Deposition−Precipitation. In *Handbook of Heterogeneous Catalysis*; Ertl, G., Knözinger, H., Schüth, F., Weitkamp, J., Eds.; Wiley VCH: Weinheim, Germany, 2008; pp 428−467.
(41) Mutz, B.; Carvalho, H. W. P.; Kleist, W.; Grunwaldt, J. D. *J. Phys.: Conf. Ser.* **2016**, *712*, 012050.
(42) van der Lee, M. K.; van Dillen, J.; Bitter, J. H.; de Jong, K. P. *J. Am. Chem. Soc.* **2005**, *127*, 13573−13582.
(43) de Jong, K. P. Deposition Precipitation. In *Synthesis of Solid Catalysts*, de Jong, K. P., Ed.; Wiley VCH: Weinheim, Germany, 2009; pp 111−134.
(44) Bergeret, G.; Gallezot, P., Particle Size and Dispersion Measurements. In *Handbook of Heterogeneous Catalysis*, Ertl, G.; Knözinger, H.; Schüth, F.; Weitkamp, J., Eds.; Wiley VCH: Weinheim, Germany, 2008; pp 738−765.
(45) Belimov, M. Methane production from co electrolysis products applying a microchannel reactor. Ph.D. Dissertation in preparation, IMVT, Karlsruhe Institute of Technology, 2017.
(46) Koschany, F.; Schlereth, D.; Hinrichsen, O. *Appl. Catal., B* **2016**, *181*, 504−516.
(47) Kopyscinski, J.; Schildhauer, T. J.; Vogel, F.; Biollaz, S. M. A.; Wokaun, A. *J. Catal.* **2010**, *271*, 262−279.
(48) Zhang, J.; Fatah, N.; Capela, S.; Kara, Y.; Guerrini, O.; Khodakov, A. Y. *Fuel* **2013**, *111*, 845−854.
(49) Liu, J.; Li, C.; Wang, F.; He, S.; Chen, H.; Zhao, Y.; Wei, M.; Evans, D. G.; Duan, X. *Catal. Sci. Technol.* **2013**, *3*, 2627−2633.
(50) Razzaq, R.; Zhu, H.; Jiang, L.; Muhammad, U.; Li, C.; Zhang, S. *Ind. Eng. Chem. Res.* **2013**, *52*, 2247−2256.
(51) Rahmani, S.; Rezaei, M.; Meshkani, F. *J. Ind. Eng. Chem.* **2014**, *20*, 1346−1352.
(52) Chicinaş, I.; Pop, V.; Isnard, O.; Le Breton, J. M.; Juraszek, J. *J. Alloys Compd.* **2003**, *352*, 34−40.
(53) Sitthisa, S.; An, W.; Resasco, D. E. *J. Catal.* **2011**, *284*, 90−101.
(54) Wang, G.; Jin, Y.; Liu, G.; Li, Y. *Energy Fuels* **2013**, *27*, 4448−4456.
(55) de Faria, D. L. A.; Venâncio Silva, S.; de Oliveira, M. T. *J. Raman Spectrosc.* **1997**, *28*, 873−878.
(56) Ospitali, F.; Sabetta, T.; Tullini, F.; Nannetti, M. C.; Di Lonardo, G. *J. Raman Spectrosc.* **2005**, *36*, 18−23.
(57) D'Ippolito, V.; Andreozzi, G. B.; Bersani, D.; Lottici, P. P. *J. Raman Spectrosc.* **2015**, *46*, 1255−1264.
(58) Nasibulin, A. G.; Rackauskas, S.; Jiang, H.; Tian, Y.; Mudimela, P. R.; Shandakov, S. D.; Nasibulina, L. I.; Jani, S.; Kauppinen, E. I. *Nano Res.* **2009**, *2*, 373−379.
(59) Baghaie Yazdi, M.; Choi, K. Y.; Wulferding, D.; Lemmens, P.; Alff, L. *New J. Phys.* **2013**, *15*, 103032.
(60) Abelló, S.; Bolshak, E.; Montané, D. *Appl. Catal., A* **2013**, *450*, 261−274.
(61) Abelló, S.; Bolshak, E.; Gispert Guirado, F.; Farriol, X.; Montané, D. *Catal. Sci. Technol.* **2014**, *4*, 1111−1122.
(62) Chan, S. S.; Wachs, I. E. *J. Catal.* **1987**, *103*, 224−227.
(63) Vuurman, M. A.; Stufkens, D. J.; Oskam, A.; Deo, G.; Wachs, I. E. *J. Chem. Soc., Faraday Trans.* **1996**, *92*, 3259−3265.
(64) Hu, D.; Gao, J.; Ping, Y.; Jia, L.; Gunawan, P.; Zhong, Z.; Xu, G.; Gu, F.; Su, F. *Ind. Eng. Chem. Res.* **2012**, *51*, 4875−4886.
(65) Huang, D.; Ke, M.; Bao, X.; Liu, H. *Ind. Eng. Chem. Res.* **2016**, *55*, 1192−1201.
(66) Wang, L.; Li, D.; Koike, M.; Koso, S.; Nakagawa, Y.; Xu, Y.; Tomishige, K. *Appl. Catal., A* **2011**, *392*, 248−255.
(67) Mears, D. E. *J. Catal.* **1971**, *20*, 127−131.
(68) Wakao, N.; Kaguei, S.; Funazkri, T. *Chem. Eng. Sci.* **1979**, *34*, 325−336.
(69) Froment, G. F.; Bischoff, K. B.; De Wilde, J. *Chemical Reactor Analysis and Design*, 3rd ed.; John Wiley & Sons, Inc.: Hoboken, NJ, 2011; pp 154−239.
(70) Romkes, S. J. P.; Dautzenberg, F. M.; van den Bleek, C. M.; Calis, H. P. A. *Chem. Eng. J.* **2003**, *96*, 3−13.
(71) Berger, R. *EUROKIN fixed bed html, EUROKIN spreadsheet on requirements for measurement of intrinsic kinetics in the gas solid fixed bed reactor*2012. Available at the following: http://eurokin.org/wp content/uploads/downloads/2012/08/EUROKIN fixed bed html guide.pdf.
(72) Bian, L.; Zhang, L.; Xia, R.; Li, Z. *J. Nat. Gas Sci. Eng.* **2015**, *27*, 1189−1194.
(73) Li, Y.; Zhang, Q.; Chai, R.; Zhao, G.; Liu, Y.; Lu, Y.; Cao, F. *AIChE J.* **2015**, *61*, 4323−4331.
(74) Aziz, M. A. A.; Jalil, A. A.; Triwahyono, S.; Mukti, R. R.; Taufiq Yap, Y. H.; Sazegar, M. R. *Appl. Catal., B* **2014**, *147*, 359−368.
(75) Ocampo, F.; Louis, B.; Kiwi Minsker, L.; Roger, A. C. *Appl. Catal., A* **2011**, *392*, 36−44.
(76) Cai, M.; Wen, J.; Chu, W.; Cheng, X.; Li, Z. *J. Nat. Gas Chem.* **2011**, *20*, 318−324.
(77) Ocampo, F.; Louis, B.; Roger, A. C. *Appl. Catal., A* **2009**, *369*, 90−96.
(78) He, S.; Li, C.; Chen, H.; Su, D.; Zhang, B.; Cao, X.; Wang, B.; Wei, M.; Evans, D. G.; Duan, X. *Chem. Mater.* **2013**, *25*, 1040−1046.
(79) Abelló, S.; Berrueco, C.; Montané, D. *Fuel* **2013**, *113*, 598−609.
(80) Du, G.; Lim, S.; Yang, Y.; Wang, C.; Pfefferle, L.; Haller, G. L. *J. Catal.* **2007**, *249*, 370−379.
(81) Barrientos, J.; Lualdi, M.; Suárez París, R.; Montes, V.; Boutonnet, M.; Järås, S. *Appl. Catal., A* **2015**, *502*, 276−286.
(82) Butt, J. B.; Petersen, E. E. Deactivation by Fouling. *Activation, Deactivation, and Poisoning of Catalysts*; Academic Press Inc.: San Diego, 1988; pp 63−120.
(83) McCarty, J. G.; Wise, H. *J. Catal.* **1979**, *57*, 406−416.
(84) Gardner, D. C.; Bartholomew, C. H. *Ind. Eng. Chem. Prod. Res. Dev.* **1981**, *20*, 80−87.
(85) Bartholomew, C. H. *Catal. Rev.: Sci. Eng.* **1982**, *24*, 67−112.
(86) Bartholomew, C. H. *Appl. Catal., A* **2001**, *212*, 17−60.
(87) Gnanamani, M. K.; Shafer, W. D.; Sparks, D. E.; Davis, B. H. *Catal. Commun.* **2011**, *12*, 936−939.
(88) Martinelli, M.; Visconti, C. G.; Lietti, L.; Forzatti, P.; Bassano, C.; Deiana, P. *Catal. Today* **2014**, *228*, 77−88.
(89) Grunwaldt, J. D.; Molenbroek, A. M.; Topsøe, N. Y.; Topsøe, H.; Clausen, B. S. *J. Catal.* **2000**, *194*, 452−460.
(90) Newton, M. A. *Chem. Soc. Rev.* **2008**, *37*, 2644−2657.
(91) Grunwaldt, J. D.; Schroer, C. G. *Chem. Soc. Rev.* **2010**, *39*, 4741−4753.
(92) Grunwaldt, J. D.; Wagner, J. B.; Dunin Borkowski, R. E. *ChemCatChem* **2013**, *5*, 62−80.

(93) Eslava, J. L.; Iglesias Juez, A.; Agostini, G.; Fernández García, M.; Guerrero Ruiz, A.; Rodríguez Ramos, I. *ACS Catal.* **2016**, *6*, 1437−1445.
(94) Ferrari, A. C.; Robertson, J. *Phys. Rev. B: Condens. Matter Mater. Phys.* **2000**, *61*, 14095.
(95) Sadezky, A.; Muckenhuber, H.; Grothe, H.; Niessner, R.; Pöschl, U. *Carbon* **2005**, *43*, 1731−1742.
(96) Lovell, E. C.; Fuller, A.; Scott, J.; Amal, R. *Appl. Catal., B* **2016**, *199*, 155−165.